

# Space squeezing optics: performance limits and implementation at microwave frequencies

## – Supplementary Information

Michal Mrnka,<sup>1,\*</sup> Euan Hendry,<sup>1</sup> Jaroslav Láćík,<sup>2</sup> Rachel A. Lennon,<sup>1</sup> Lauren E. Barr,<sup>1</sup> Ian Hooper,<sup>1</sup> and David B. Phillips<sup>1</sup>

<sup>1</sup>School of Physics and Astronomy, University of Exeter, Exeter, EX4 4QL, UK.

<sup>2</sup>Department of Radio Electronics, Brno University of Technology, 616 00 Brno, Czech Republic.

This supplementary document provides further, in-depth information on the theory, various trade-offs and design of the Fabry-Pérot cavity based spaceplate. The experimental setup and methods used to characterise the spaceplate are explained here. In the last section we include information on the design and performance of a stochastic spaceplate consisting of three coupled resonators.

### §1 A Fabry-Pérot resonator as a spaceplate

It has been shown that the angular dispersion in a Fabry-Pérot cavity can be used to design a spaceplate [1]. Here, we analyze such a solution from a general point of view and find the trade-off between the compression ratio ( $\mathcal{C}$ ), numerical aperture (NA) and bandwidth ( $\delta\omega$ ) of the spaceplate. In addition we show how the compression ratio can be obtained from the Q factor of the resonator or reflectances of its mirrors.

The transmission coefficient of a Fabry-Pérot cavity made of two semitransparent mirrors with equal reflectance ( $R_1 = R_2 = R$ ) separated by a distance  $d_{SP}$  is

$$t(\theta, \omega) = \frac{t_1 t_2 \exp(i\beta)}{1 + r_1 r_2 \exp(2i\beta)}, \quad (1)$$

with

$$\beta = \frac{2\pi}{\lambda} d_{SP} \cos \theta = \frac{\omega}{c} d_{SP} \cos \theta, \quad (2)$$

where  $R = r^2$  and  $r_1, r_2, t_1, t_2$  are the reflection and transmission coefficients of the mirrors (Stokes relations  $r_1 = -r_2$ ,  $t_1 t_2 = 1 - r^2$ ),  $\lambda$  is the free space wavelength,  $\theta$  is the incidence angle and  $\omega$  is the angular frequency. We assume all the regions are free space (see Fig. 1).

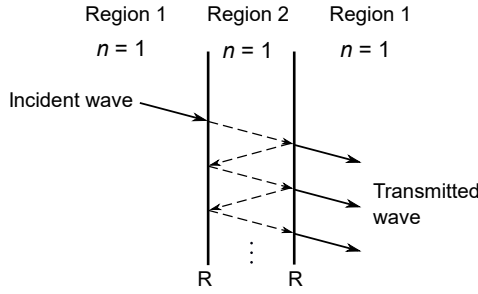


FIG. 1. Fabry-Pérot cavity formed by two mirrors with equal reflectances  $R$ .

#### 1.1 Even Fabry-Pérot resonances

The interesting behavior for a single FP resonator spaceplate occurs near the transmission peaks where the conditions for constructive interference are met. The relative phase shift between two successive reflections defining the constructive interference is  $2\beta = 2\pi\ell$ , where  $\ell$  is the order of the resonance ( $\ell = 1, 2, 3, \dots$ ). If we consider a cavity

---

\* M.Mrnka@exeter.ac.uk

with thickness  $d_{\text{SP}} = \lambda_{r1}/2$ , where  $\lambda_{r1} = 2\pi c/\omega_{r1}$  is the resonant wavelength of the first interference peak at normal incidence (i.e.  $\theta = 0^\circ$ ), we can tie the resonance of the structure to the interference condition as follows:

$$2\beta = 2\pi\ell \rightarrow 2\frac{2\pi}{\lambda_r(\ell, \theta)}d_{\text{SP}} \cos\theta = 2\pi\ell \rightarrow \frac{\omega_r(\ell, \theta)}{c} \frac{2\pi c}{\omega_{r1}} \cos(\theta) = 2\pi\ell. \quad (3)$$

The dispersion equation relating the resonant frequency  $\omega_r(\ell, \theta)$  corresponding to the angle  $\theta$  and resonance order  $\ell$  with respect to the normal incidence (and  $\ell = 1$ ) resonance  $\omega_{r1}$ :

$$\omega_r(\ell, \theta) = \frac{\ell}{\cos\theta} \omega_{r1}. \quad (4)$$

The resonant frequency of the FP cavity thus shifts with  $1/\cos\theta$ . However, for small angles in can be approximated by the first two terms of its Taylor expansion:

$$1/\cos\theta \sim 1 + \frac{1}{2}\theta^2. \quad (5)$$

Equation 4 tells us that the higher order (even) resonant modes ( $\ell > 1$ ) are more sensitive to the incidence angle by a factor  $\ell$  (see Fig. 2). This suggests that they provide a limited NA compared to the first one ( $\ell = 1$ ), however as we show later, the compression ratio  $\mathcal{C}$  remains the same. Effectively, this means that a resonator operating in its higher resonance can substitute a thicker slab of air but over a reduced angular range.

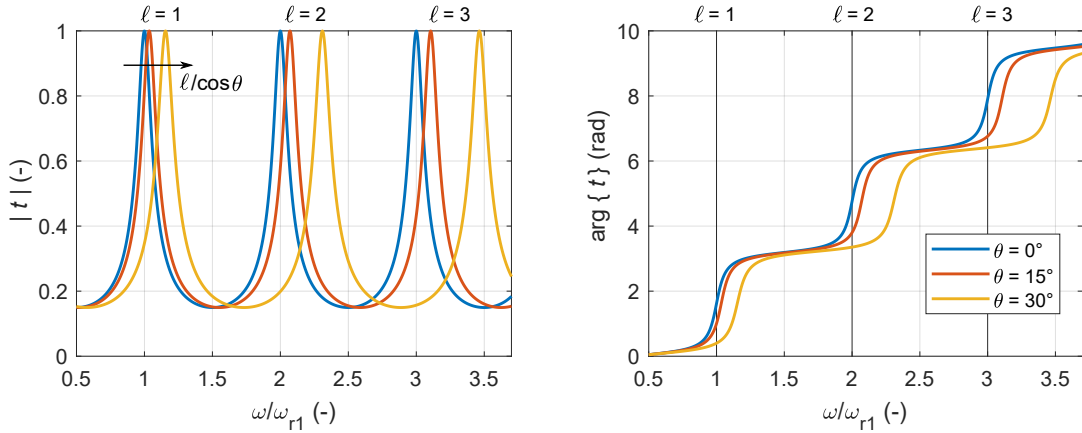


FIG. 2. First three even resonances and their shift with incidence angle - magnitude (left) and phase (right) of the transmission coefficient. The shift of  $\ell^{\text{th}}$  order with angle  $\theta$  is given by  $\ell/\cos\theta$

Now, we evaluate the phase of the transfer function of the spaceplate given by the dispersion according to eq. (4). To do this, we use a group delay (GD) concept described in section 1.2. We linearize the phase of the spaceplate about the resonance and the slope of the linear portion of the phase is considered to be the approximate GD.

Figure 3 shows that the resonance of the spaceplate shifts with the incidence angle as  $\ell/\cos\theta$ . The phase  $\phi_{\text{SP}}(\theta)$  is the phase difference (over the length of the SP) between  $\theta = 0^\circ$  and  $\theta > 0^\circ$  angles. This phase can be found from the triangle in Fig. 3 and is given as:

$$\phi_{\text{SP}}(\theta) = -\ell \frac{GD}{\cos\theta}. \quad (6)$$

## 1.2 Compression factor of the spaceplate, $\mathcal{C}$ , and the properties of the FP resonator

The transmission curve of a resonator based spaceplate is fully given by its quality factor (Q-factor) and the order of the resonance  $\ell$ . The compression factor  $\mathcal{C}$  can be determined from the fundamental properties of the resonator (under certain assumptions) as follows.

If we consider an FP cavity formed by 2 mirrors with identical reflectance  $R$  and assuming:

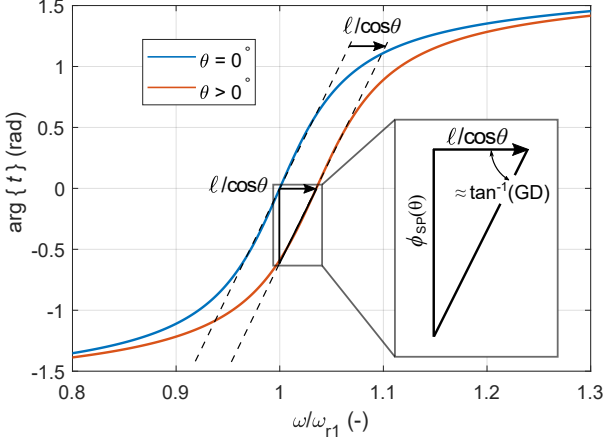


FIG. 3. Phase profile of the SP as a function of normalized angular frequency close to the 1<sup>st</sup> resonance. Blue curve represents normal incidence - the phase profile of the resonance is shifted by  $\ell/\cos\theta$  (where  $\ell=1$ ) for incidence angle  $\theta > 0^\circ$ , plotted in red. The change in phase ( $\arg\{t\}$ ) related to the change of incidence angle  $0 \rightarrow \theta$  at operating frequency  $\omega/\omega_{r1} = 1$  is  $\phi_{SP}(\theta)$ .

- $R$  does not depend on the angle of incidence  $\theta$ , and
- the phase of the transmission coefficient is linear about the resonance (see Fig. 4),

then the slope of the linearised phase determines the group delay of the structure

$$GD_{SP} = \frac{d\phi}{d\omega} \approx \frac{\Delta\phi}{\Delta\omega} = \frac{\pi/2}{2\pi\Delta f} = \frac{1}{4\Delta f} = \frac{Q}{4f_r} = \frac{\pi Q}{2\omega_r}, \quad (7)$$

which must not change with the incidence angle and  $\Delta f = \Delta\omega/2\pi$  is the line width of the resonator under normal incidence,  $f_r = \omega_r/2\pi$  is the resonant frequency and the Q-factor is defined by  $Q = f_r/\Delta f = \omega_r/\Delta\omega$ .

The group delay in free space of effective thickness  $d_{eff}$  which the spaceplate is to substitute is:

$$GD_{FS} = \frac{d\phi}{d\omega} = \frac{d}{d\omega} \left( \frac{\omega}{c} d_{eff} \right) = \frac{d_{eff}}{c}. \quad (8)$$

Thus, by assuming  $GD_{SP} = GD_{FS}$  we obtain the equivalent thickness of free space,  $d_{eff}$ , our resonator can substitute:  $d_{eff} = c \cdot \pi Q / (2\omega_r) = \lambda_r Q / 4$ .

If we operate the spaceplate of thickness  $d_{SP} = \ell\lambda_r/2$  at a frequency that matches the resonant frequency of the resonator  $f = f_r$  the transmission for the normal incidence is 1 and it slowly tapers off with incidence angle. The compression factor  $C$  in this case is given as:

$$C = \frac{d_{eff}}{d_{SP}} = \frac{\frac{\lambda_r Q}{4}}{\ell \frac{\lambda_r}{2}} = \frac{Q}{2\ell}. \quad (9)$$

Assuming a high reflectance ( $R$ ) of the mirrors that form the cavity (such as  $1 - R \ll 1$ ) we can tie the Q-factor to the reflectance as [2]

$$Q = -\frac{\pi\ell}{\ln R}, \quad (10)$$

which combined with eq. 9 leads to the compression factor as a function of the reflectance of the mirrors:

$$C = -\frac{\pi}{2\ln R}. \quad (11)$$

Under the assumptions given above, we can see that the compression factor  $C$  of the FP resonator spaceplate does not depend on the order of the resonance  $\ell$ . However, we should keep in mind that the higher resonances will offer a

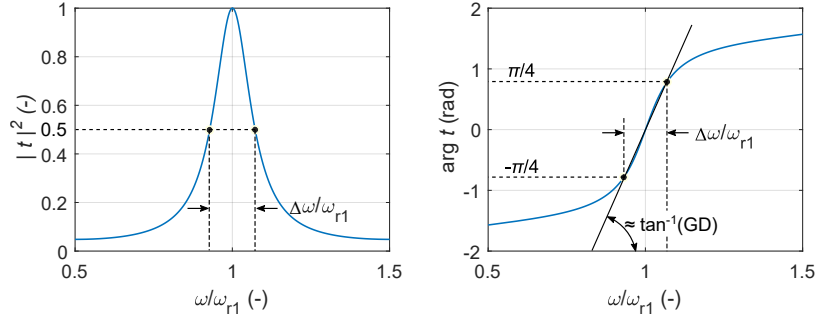


FIG. 4. Resonance line of a cavity with half wavelength thickness. The frequency bandwidth (full width at half maximum) is shown in the figures.

reduced NA (see eq. (4)).

### 1.3 Numerical aperture and bandwidth of the FP resonator spaceplate

As shown below, there is a fundamental trade-off between the compression ratio, the numerical aperture of the spaceplate, and the frequency bandwidth it can operate over.

Starting with monochromatic waves, if we allow the transmittance of the spaceplate at normal incidence to be half of the maximum, the NA is maximized. The angles  $\theta_1$  and  $\theta_2$  describe the angles where the transmittance is increased to 1 (angle  $\theta_1$ ) and where it drops to 0.5 again (angle  $\theta_2$ ). In this case, the angle  $\theta_2$  defines the  $NA = \sin \theta_2$ . The operating angular frequency is  $\omega_{\text{work}} = \omega_r + \Delta\omega/2$  (see Fig. 5).

If we wish to have the transmittance at normal incidence equal to 1, the numerical aperture is given by the  $\theta_1$  angle,  $NA = \sin \theta_1$  (operating frequency  $\omega_{\text{work}} = \omega_r$ ).

The angles  $\theta_1$  and  $\theta_2$  are given as follows:

$$\theta_1 = \cos^{-1} \frac{\omega_r}{\omega_r + \Delta\omega/2} = \cos^{-1} \frac{1}{1 + 1/2Q} = \cos^{-1} \frac{1}{1 + 1/4C\ell}, \quad (12)$$

$$\theta_2 = \cos^{-1} \frac{\omega_r}{\omega_r + \Delta\omega} = \cos^{-1} \frac{1}{1 + 1/Q} = \cos^{-1} \frac{1}{1 + 1/2C\ell}. \quad (13)$$

The numerical aperture for the case with transmittance at normal incidence equal to 0.5 can be written using the trigonometric identity  $\sin(\cos^{-1}(x)) = \sqrt{1 - x^2}$

$$NA = \sin \theta_2 = \sqrt{1 - \left( \frac{1}{1 + 1/Q} \right)^2} = \sqrt{1 - \left( \frac{1}{1 + 1/2C\ell} \right)^2}, \quad (14)$$

and it can be easily modified for the case with unity transmittance at  $0^\circ$ ,  $NA = \sin \theta_1$ .

Now, we turn our attention from monochromatic waves and introduce a signal with a certain angular frequency bandwidth  $\delta\omega = \omega_{\max} - \omega_{\min}$  and due to the nature of the spaceplate we must assume  $\delta\omega < \Delta\omega$  (if we do not want to compromise on the performance even more than shown in Fig. 5). This effectively means that the maximum acceptable frequency shift of the resonance, which is  $\Delta\omega$  for monochromatic waves will be reduced to  $\Delta\omega - \delta\omega$ . Using the dispersion equation (eq. (4)) the maximum angle  $\theta_2$  is

$$\theta_2 = \cos^{-1} \frac{\omega_r}{\omega_r + \Delta\omega - \delta\omega} = \cos^{-1} \frac{1}{1 + 1/Q - \delta\omega/\omega_r} = \cos^{-1} \frac{1}{1 + 1/2C\ell - \delta\omega/\omega_r}, \quad (15)$$

and the NA of the spaceplate with given guaranteed frequency bandwidth  $\delta\omega$  is

$$NA = \sin \theta_2 = \sqrt{1 - \left( \frac{1}{1 + 1/Q - \delta\omega/\omega_r} \right)^2} = \sqrt{1 - \left( \frac{1}{1 + 1/2C\ell - \delta\omega/\omega_r} \right)^2}. \quad (16)$$

The equation 16 can be rearranged for the approximate fractional bandwidth:

$$\delta\omega/\omega_r = 1 + \frac{1}{2C\ell} - \frac{1}{\sqrt{-NA^2 + 1}}, \quad (17)$$

where  $0 \leq \delta\omega/\omega_r \leq 1/2C\ell$  interval bounds the feasible solutions. It enforces that the bandwidth is a positive quantity  $0 \leq \delta\omega/\omega_r$  and that we work sufficiently close to the resonance  $\delta\omega/\omega_r \leq 1/2C\ell$  to cap the maximum allowed transmission loss at 0.5. We call the  $\delta\omega/\omega_r$  quantity an "approximate" fractional bandwidth as the  $\omega_r$  frequency is not at the centre of the band  $\delta\omega$ . The equations are very accurate for high Q cavities, but still work well for lower Q cases ( $R \approx 0.5$ ).

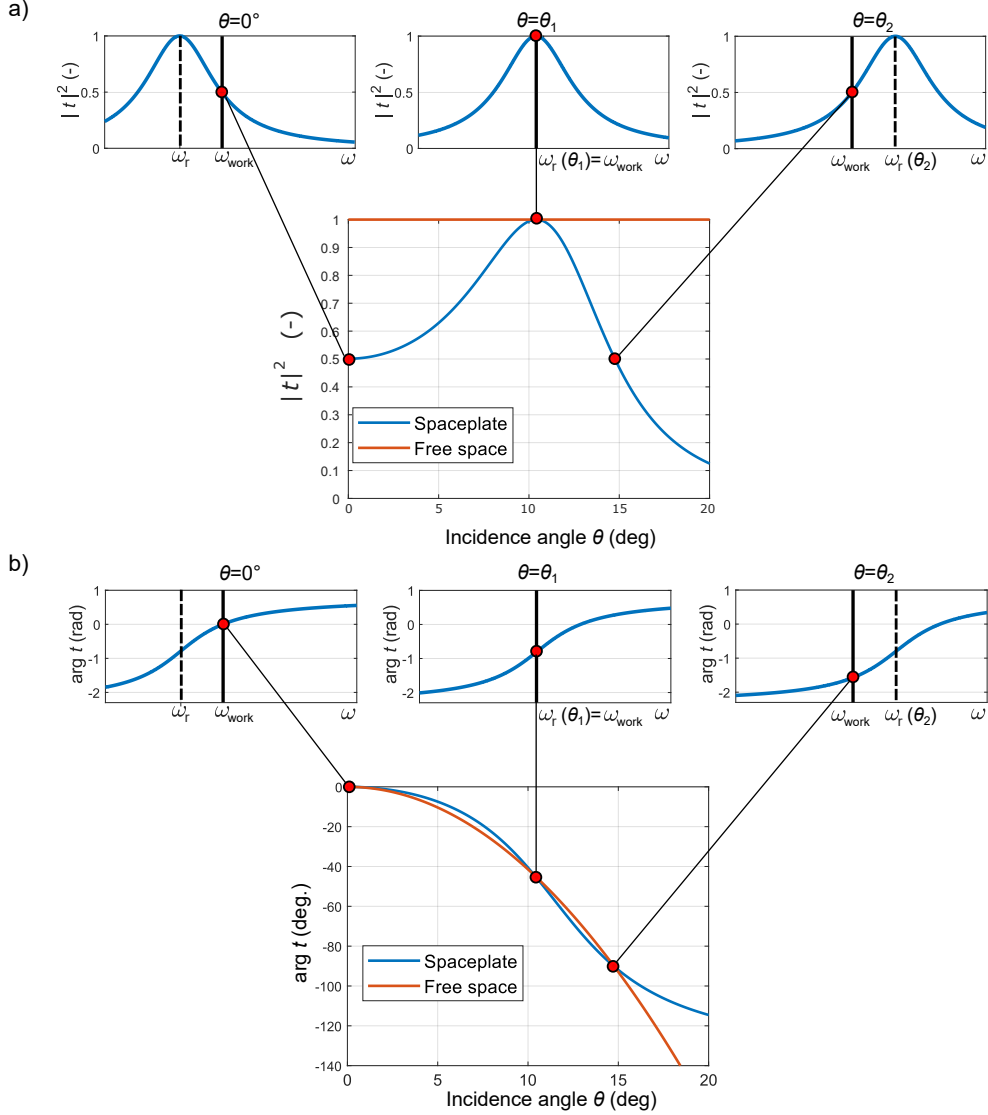


FIG. 5. Operation of the spaceplate explained using how the amplitude (a) and phase (b) of the transfer function depend on the resonance shift of the FP cavity with the incidence angle. This case corresponds to the maximum NA, where the transmittance at normal incidence is reduced to 0.5. The operating angular frequency is  $\omega_{work} = \omega_r + \Delta\omega/2$ , where  $\omega_r$  is the resonant frequency at normal incidence. The important angles  $\theta_1$  and  $\theta_2$  are shown here.

#### 1.4 Interesting trade-offs

Equations (9), (11), (14) and (16) are useful for studying the performance trade-offs and the limits of FP resonator spaceplates. To do so, we sweep the reflectance of the mirrors  $R$  in the range 0.5 to 0.99 and plot the compression factor as a function of  $R$  (see Fig. 6a) and as a function of the Q-factor of the cavity (see Fig. 6b). The insets show

the compression factor  $\mathcal{C}$  for even higher reflectances ranging from 0.99 up to 0.9999. In limiting case, for  $Q \rightarrow \infty$  (also  $R \rightarrow \infty$ ), the compression ratio will tend to infinity (see eq. (9)) as the NA will be approaching 0 (eq. (14)):

$$\lim_{Q \rightarrow +\infty} \mathcal{C} = \infty \quad \lim_{Q \rightarrow +\infty} NA = 0 \quad (18)$$

An important trade-off for a resonant spaceplate is that between the numerical aperture (or maximum incidence angle  $\theta_{\max}$ ), the compression factor and the bandwidth ( $\delta\omega$ ). In Fig. 6c we can see the maximum acceptance angle (transmittance = 0.5 at normal incidence) as a function of the compression factor with the bandwidth as a parameter. The bandwidth is expressed as a fraction of the spectral linewidth of the resonator  $\Delta\omega$ . The blue curve ( $\delta\omega = 0$ ) represents a monochromatic wave and thus sets the upper bound on achievable numerical aperture. As the bandwidth increases the NA goes down. The maximum theoretical bandwidth (i.e.  $\delta\omega = \Delta\omega$ ) does not allow for any shift of the resonance and thus results in  $NA = 0$ . The inset in Fig. 6c shows that a compression factor of  $\mathcal{C} = 3282$  can be achieved with FP resonator spaceplate within NA corresponding to  $\theta_{\max} = 1^\circ$ , and  $\mathcal{C} = 13130$  within  $\theta_{\max} = 0.5^\circ$ .

It has been mentioned that the spaceplate trades off its numerical aperture for the transmittance at normal incidence (Fig. 5a). Figure 2 of the main paper shows that this depends on the selection of the operating frequency  $\omega_{\text{work}}$ . If we choose to operate at resonance frequency  $\omega_{\text{work}} = \omega_r$  we achieve maximum transmittance  $|t|^2 = 1$  at normal incidence, which tapers off to  $|t|^2 = 0.5$  at incidence angle  $\theta_1$ . On the other hand, if we pick  $\omega_{\text{work}} = \omega_r + \Delta\omega/2$ , the transmittance at normal incidence is  $|t|^2 = 0.5$ , increases to  $|t|^2 = 1$  (at  $\theta_1$ ), and again drops to  $|t|^2 = 0.5$  at incidence angle  $\theta_2$ . In Fig. 6d we can see the drop in normal incidence transmittance as a function of maximum incidence angle  $\theta_{\max}$ . The red axis demonstrates a real world scenario of a resonant spaceplate based on mirrors with  $R = 0.9$  and a compression factor  $\mathcal{C} = 14.9$  - here we can see that by allowing  $|t|^2 = 0.5$  at normal incidence we can increase the NA angle from  $\theta_{\max} = 10.5^\circ$  to  $\theta_{\max} = 14.8^\circ$ . Finally, the blue axis in Fig. 6d relates the range of maximum angles to the selection of operating frequency  $\omega_{\text{work}}$ .

Even though the resonance order  $\ell$  does not influence the maximum compression ratio of a spaceplate, it has a negative effect on its achievable numerical aperture (see eq. (4)). In Fig. 7 we examine this effect for  $\ell = 1$  to  $\ell = 5$ . The main benefit of operating the spaceplate at a higher order resonance is the increase in effective thickness  $d_{\text{eff}}$  since the length of the resonator is increased  $d_{\text{SP}} = \ell \cdot \lambda/2$  and the compression factor remains the same,  $d_{\text{eff}} = \mathcal{C} \cdot d_{\text{SP}}$ . The second benefit is the mechanical simplicity with low weight and costs. The spaceplate consists of only three components - two dichroic mirrors separated by free space.

## §2 Metamaterial properties of perforated metal layers

The electromagnetic interaction between light and the metal is driven by the free electrons of the metal, which give rise to a negative permittivity for frequencies below their plasma frequencies. It has been shown that one can mimic the negative permittivity of a metal near its plasma frequency by structuring the surface of a (near) perfect conductor by introducing periodic arrays of subwavelength holes. Such a structured layer of highly conducting material can support surface plasmon-like surface modes at frequencies well below the plasma frequency of the conductor [3–6], and also have the property of partial reflectance, similar to that of thin (less than the skin depth) metal films [7].

In this paper, we use highly conducting sheets with two-dimensional arrays of subwavelength, open holes to mimic the partially reflecting mirrors of a Fabry Pérot cavity. It is important that perforated layers are non diffracting, which is the case when the wavelength of radiation is larger than the period of the structure. Under this condition, the perforated metal behaves as homogeneous layer, and propagating plane waves are expected to be de-coupled [5], a necessary condition for a space plate. The effective, frequency dependent permittivity of such a layer is determined by the size and spacing of holes, allowing the creation of mirrors with well-controlled and near-arbitrary reflectivity. When both the perforation holes and the period of the array is significantly less than the wavelength of incident radiation, one expects a large negative effective permittivity at low frequencies, similar to that seen for homogeneous metals at frequencies well below the plasma frequency [5].

## §3 Design of a resonant spaceplate

A Fabry-Pérot resonator spaceplate can be built similarly as shown in section §5 of SI as an air (free-space) cavity surrounded by high index dielectric sheets. Indeed, this approach was proposed in [1], where the authors suggested using thin sheets of material with  $\epsilon_r = 15$  operating near the quarter wavelength resonance to maximize the reflectance of the sheets. Here, we use metallic hole arrays (described in the previous section) made of thin copper sheets to design the mirrors of the FP cavity. This approach has several practical advantages such as its low cost, reduced thickness and, most importantly, the tunability. By adjusting the filling ratio one can design a dichroic mirror with arbitrary reflectance. This in turn gives direct and continuous control over the Q-factor of the

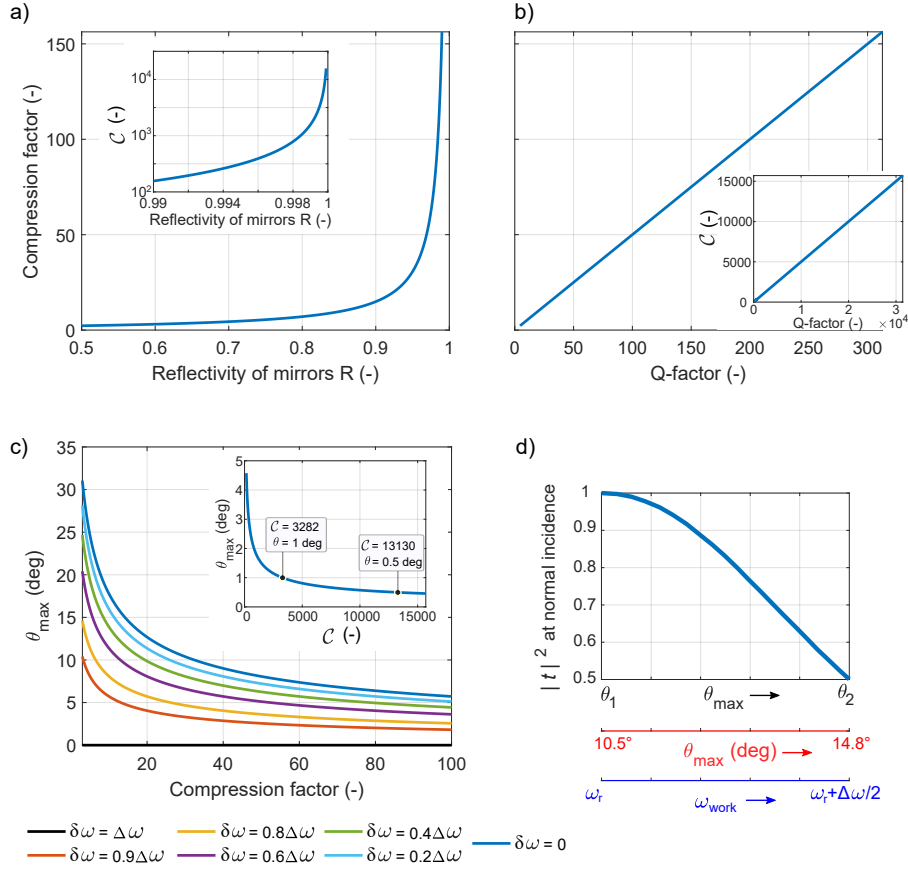


FIG. 6. Main trade-offs of a FP resonator spaceplate (with  $\ell = 1$ ).  $\delta\omega$  represents the available bandwidth and  $\Delta\omega$  is the linewidth of the resonator

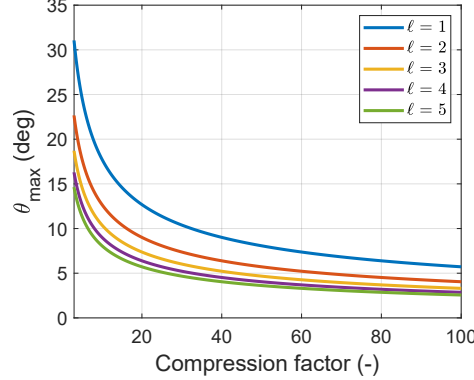


FIG. 7. Numerical aperture as a function of compression ratio for the 5 lowest order resonances, assuming monochromatic operation. The drop in NA with increasing  $\ell$  is obvious.

cavity, thus defining the compression ratio of the spaceplate. The analytical model of the hole arrays that we use to determine their reflectance was described in the previous section. The model allows us to include the angle dependent reflectance of the mirrors in eq. (1). We verify the analytical design of the spaceplate with numerical simulations in a commercial finite element software, Ansys HFSS.

### 3.1 Analysis and design of dichroic mirrors

The mirrors are implemented by etching a periodic square hole motive on a copper cladding (35  $\mu\text{m}$  thick) of a dielectric microwave substrate Rogers R4350B with thickness 1.524 mm, dielectric constant  $\varepsilon_r = 3.66$  and loss tangent

$\tan\delta = 0.0037$  (10 GHz). To achieve a reasonable trade-off among bandwidth, compression factor and NA we target a reflectance of the mirrors close to 0.8 ( $C = 7$ ). The final dimensions of the fabricated hole array sheets can be found in Fig. 8a.

We numerically analyze the hole array as a periodic structure with a unit cell shown in Fig. 8a using Ansys HFSS. First, we sweep the frequency in the range 10-40 GHz and observe the reflectance (see Fig. 8c) of one sheet. From these values, using eq. (11), we can predict the compression ratio of a single FP resonator spaceplate made of two sheets, as a function of frequency.

At operating frequency 21 GHz and normal incidence, the reflectance of the mirrors is about 0.82 which corresponds to the maximum theoretical compression factor of  $C = 7.9$ . Due to the final thickness of our dichroic mirrors deposited on dielectric substrates, the achievable compression is to be appreciably lower than the theoretical limit.

Unfortunately, the reflectance of the mirrors changes with the incidence angle in a way that differs for the two polarisation states (TE and TM). We plot this in Fig. 8d, where we sweep the incidence angle in the range of  $\theta = 0$  to 30 deg. It is obvious that the discrepancy in reflectance between the two polarisations increases with increasing incidence angle - as we show later this directly influences the performance of the SP operating with the two polarisations by slightly increasing the theoretical compression factor for TE waves while reducing it for the TM waves (see Fig. 5 of the main paper).

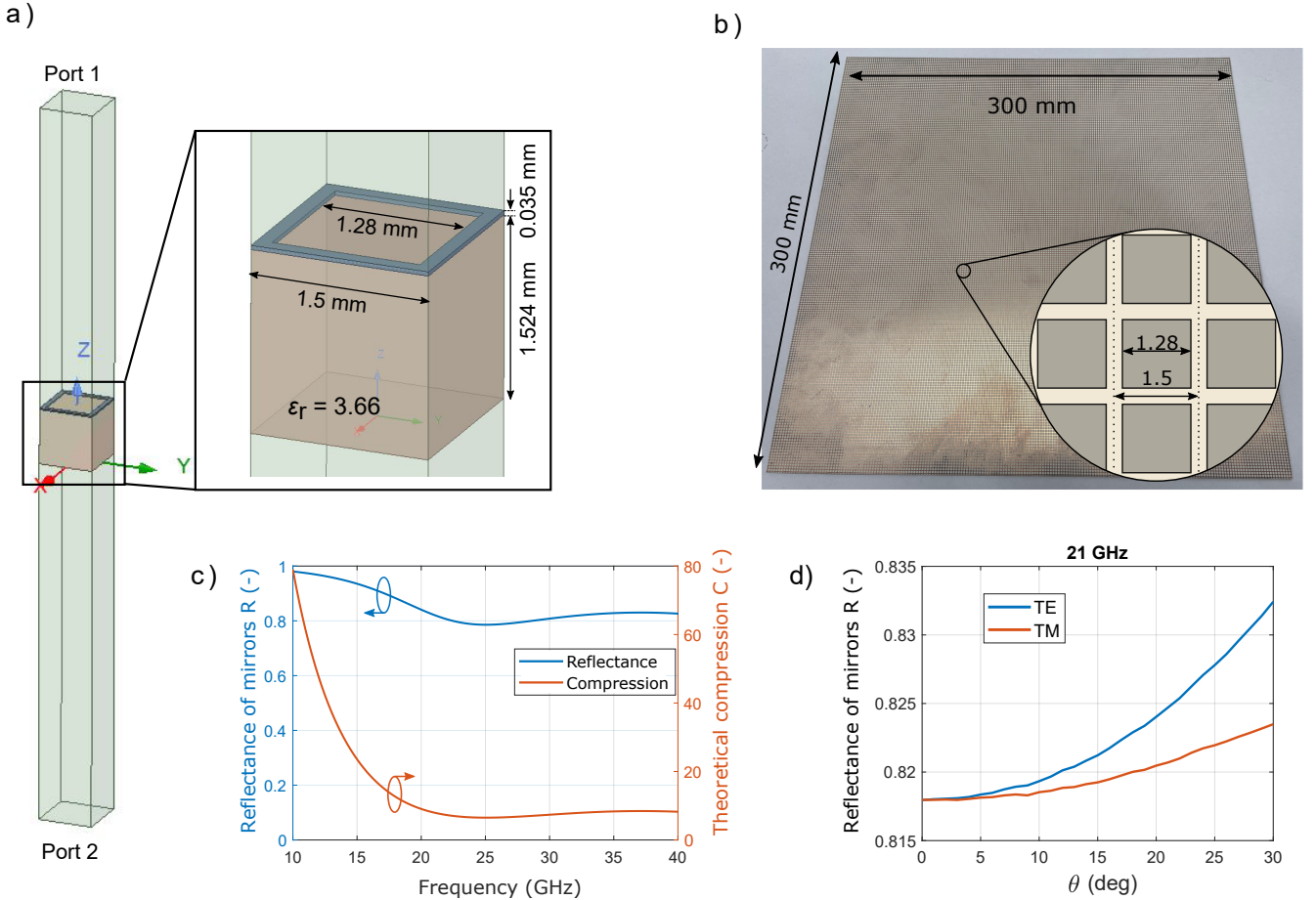


FIG. 8. a) Unit cell of the periodic mirror, Floquet ports are applied to the top and bottom area of the unit cell, all the other faces are set up as periodic boundaries. The inset shows a detail of the unit cell with dimensions. b) The photograph of the dichroic mirror used to build the spaceplate with a detail of the square unit cell c) Reflectance of the mirror and theoretically achievable compression ratio of a spaceplate based on the mirror as a function of frequency. d) Reflectance of the mirrors as a function of incidence angle for the TE and TM polarisation at 21 GHz.

### 3.2 Analysis and design of the experimental spaceplate

The experimental spaceplate is formed from a pair of dichroic mirrors described in the previous section. The lateral

size of the spaceplate is  $300 \times 300 \text{ mm}^2$ . The mirror sheets are kept apart at constant distance by 6.56 mm thick spacers resulting in resonant frequency at normal incidence of 21 GHz.

The structure is again analysed as a periodic structure with a unit cell given in Fig. 9. The simulated spectral line is compared to the measured one in Fig. 9. The experiment is described in the following section.

The simulated transmittance and the phase of the transmission coefficient are shown in Fig. 11 at five frequency points 21, 21.2, 21.4, 21.6, 21.8 GHz with  $f_r = 21 \text{ GHz}$ . Both polarisations are shown in the figures together with a free-space fit. As a result of the unequal reflectances of the mirrors for the two polarisations, the phase of TE polarisation is slightly steeper than the TM polarisation. This corresponds to a slightly higher compression ratio and a smaller NA for the TE polarisation compared to the TM case. For convenience the measurement results are also included in these plots. The measurement setup and processing are described in detail in the following section.

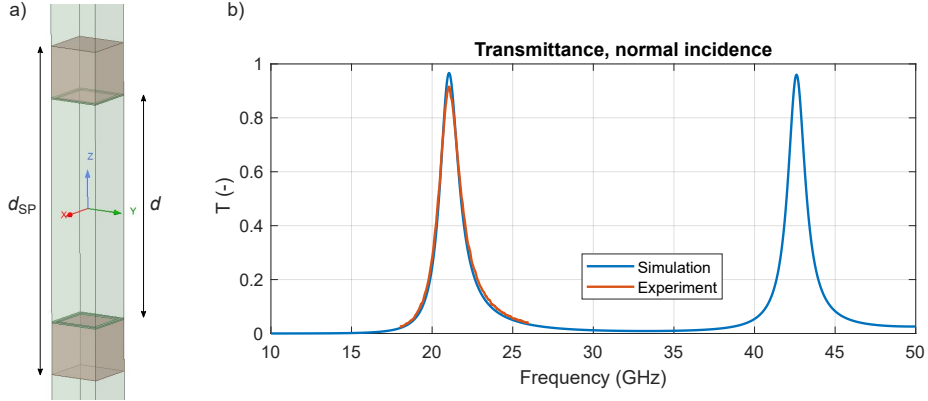


FIG. 9. a) Unit cell of the resonant spaceplate. The distance between the mirrors  $d = 6.56 \text{ mm}$  and the thickness of the spaceplate  $d_{SP}=9.618 \text{ mm}$  b) Two lowest simulated resonance lines of the FP resonator spaceplate. Measured data for the  $\ell = 1$  line is included for comparison.

## §4 Experimental setup and results

Here, we describe the two experiments we performed to validate the performance of the spaceplate. First, a dispersion measurement where we measured a plane wave response of the spaceplate under varying angle and angular frequency. Second, a field mapping, where we directly measured the effect the spaceplate has on the radius of curvature of wavefronts radiated by a point source-like antenna.

### 4.1 Dispersion measurement

The normalised transmissivity, and corresponding phase change upon transmission, of 18 to 26 GHz radiation through the spaceplate were measured as a function of the angle of incidence using a pair of Flann 810 series lens horn antennas, which have a 150 mm diameter and produce a beam with a nominal 3dB beamwidth of 5.7 and 6.6 degrees in the E- and H-planes respectively with a mid-band gain of 29.7 dBi. These were placed 1.2 m apart, with a Thorlabs HDR50/M computer controlled rotation stage placed midway between them. ABS-ASF-12 partially absorbing foam layers from ABS-Technics were placed in front of each antenna in order to reduce the influence of standing waves resulting from reflections from the front faces of the antennas (and the sample when in place). The antennas were connected to an Anritsu Vectorstar MS4647B Vector Network Analyser, and the magnitude and phase of the transmitted signal between the horn antennas was measured as a function of incident angle with the spaceplate placed upon the rotation stage. These measurements were subsequently normalised to data obtained with no sample in place, with the normalised magnitude data squared to give the transmitted intensity, and the normalised phase data giving the phase change upon transmission through the thickness of the spaceplate with respect to a slab of air with thickness equal to the spaceplate. The phase in Fig. 12, 13 and Fig. 4 of the main paper is thus calibrated to show the transmission phase of the spaceplate compared to zero thickness of air [8] - the same definition as we use in our analytical and numerical models.

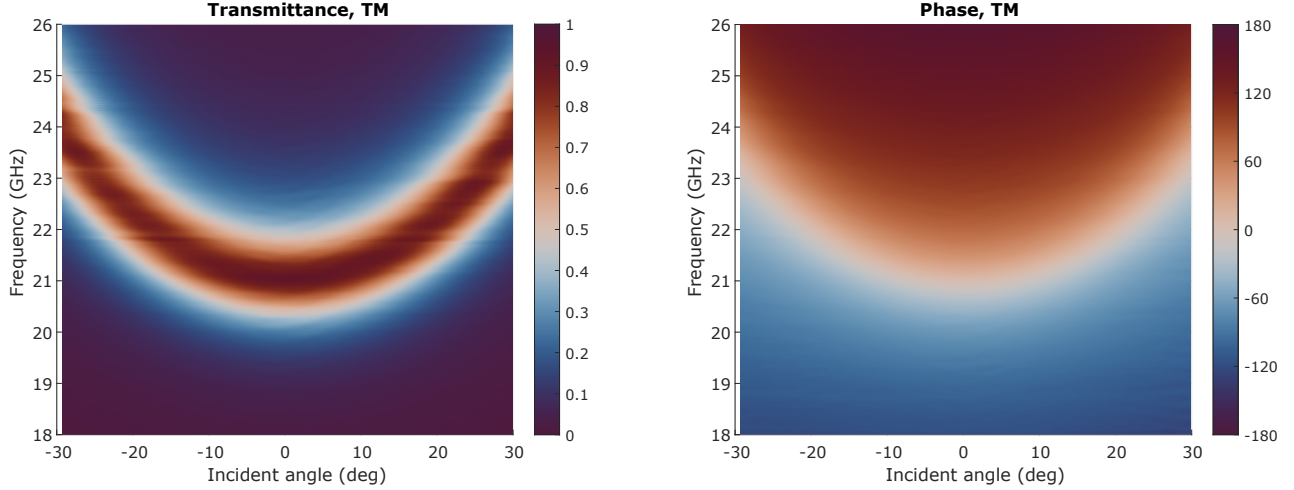


FIG. 10. Dispersion plot for TM polarisation. TE polarisation can be found in Fig. 3 of the main paper.

### 4.2 Spatial mapping of transmitted fields

To directly characterise the wavefronts, a Narda 638 standard gain horn antenna (3dB beam width of between 34 and 23 degrees across the 18 to 26 GHz band) was connected to one of the ports of an Anritsu MS4644A vector network analyser (VNA), and placed 150 mm from the front face of the spaceplate such that the radiated field impinged upon the centre of the spaceplate at (and around) normal incidence. A stripped coaxial antenna with 4 mm of protruding central conductor was connected to the 2nd port of the VNA, and mounted on a computer controlled linear translation stage at a distance of 150 mm from the back face of the spaceplate such that the protruding end of the antenna could be translated through the mid-point of the beam. The overall length of the stripped coaxial antenna and mount was sufficient that the translation stage was outside of the beam area, with microwave absorber being distributed around the volume of the beam to ensure that the measurement ensemble was minimally perturbing to the beam. The magnitude  $|t|$  and phase  $\phi_e$  of the transmission between the emitting and detecting antennas was measured across a 300 mm line through the beam centre for both TE and TM polarisations with and without the spaceplate in place.

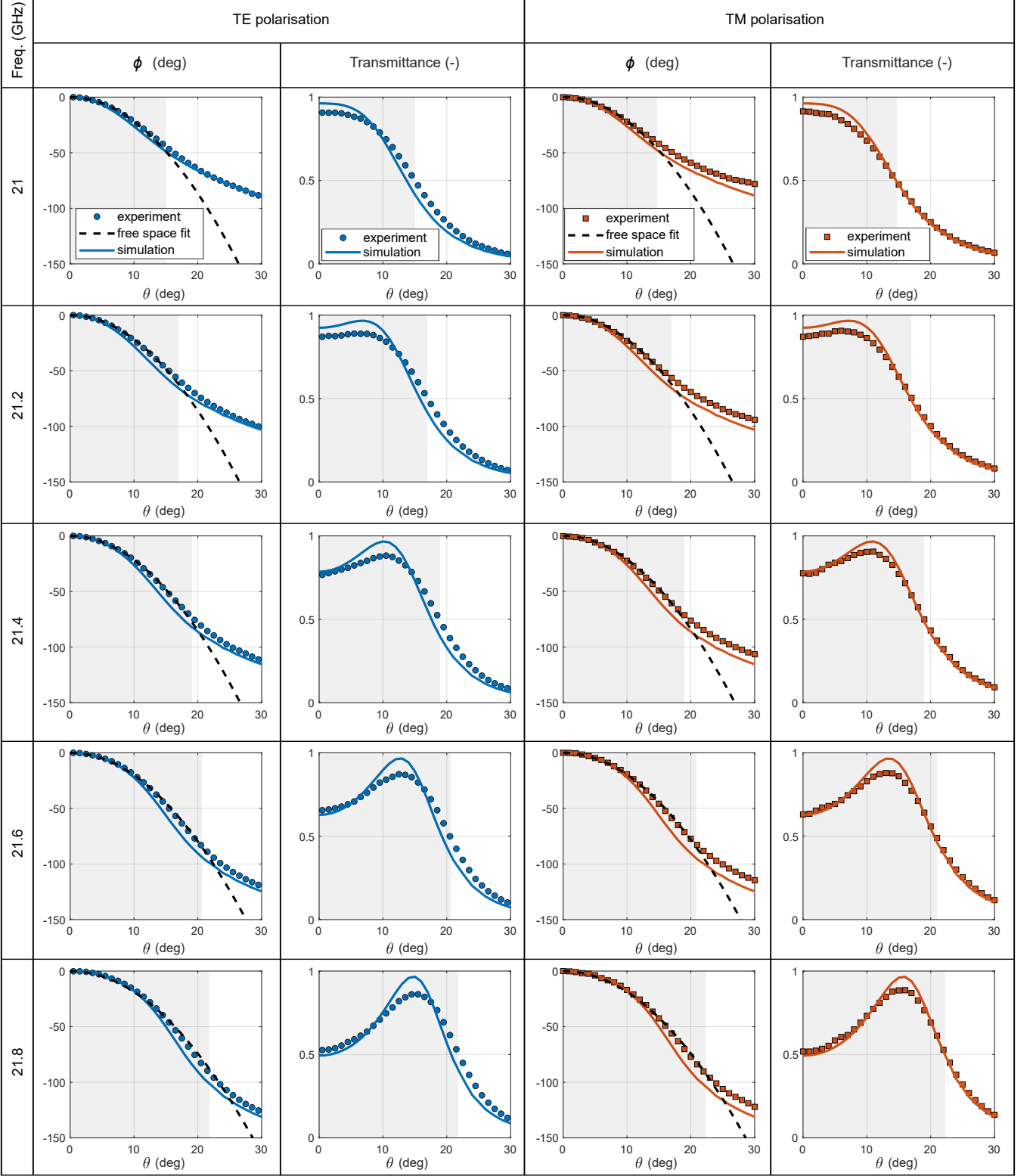


FIG. 11. Transmission phase  $\phi$  and transmittance as a function of plane wave incidence angle  $\theta$  and frequency for TE and TM polarisation. The plots compare HFSS simulation results (solid lines) with dispersion measurement results (markers) and also show a free space fit to the experimental data (dashed lines). The gray box represents the NA of the spaceplate - it is slightly smaller for the TE polarisation due to higher reflectance of the mirrors

This enabled a direct measure of the influence of the spaceplate on the wavefronts of the beam to be made (see Fig. 14).

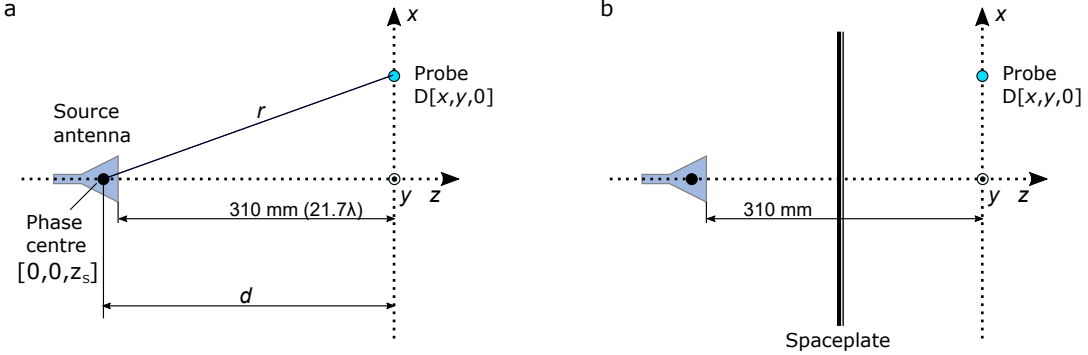


FIG. 12. Schematic view of the experimental setup for electric field scanning. Fig. a) represents the reference measurement, where the field radiated by the source antenna is measured on a plane by the detector (in fact we measure transmission coefficient  $S_{21}$  which is proportional to the electric field). In b) the spaceplate is introduced in between the source antenna and the detection plane. The radiation from the source passing through the spaceplate is measured on two orthogonal cuts  $x = 0$  and  $y = 0$ . All the dimensions are in millimeters and also relative to the free space wavelength at 21 GHz ( $\lambda = 14.3$  mm).

#### 4.3 Phase centre of an antenna and its determination

The phase centre (PC) of an antenna is the key concept in our experimental demonstration of a spaceplate and is thus described in more detail here. The phase centre can be defined as an imaginary point associated with an antenna which appears as the origin of spherical wavefronts emanating from the antenna. We present raw measured data as well as extracted positions of phase centres in a setup with and without the spaceplate - the difference is directly related to the compression factor.

Here, we briefly review how the phase centre of an antenna can be determined from the measured phase profile  $\phi_e$  (i.e.  $\arg\{S_{21}\}$ ). We demonstrate the process on phase measured along the x-axis  $\phi_e(x)$  which corresponds to the TM polarisation cut. The task can be simply defined as a search for an optimum distance  $d$  between a theoretical point source and the centre of the xy-plane where the field is sampled that minimizes the root mean square error between the theoretical  $\phi_t(x)$  and experimental phase profiles  $\phi_e(x)$ .

$$\min_d \sqrt{\frac{1}{N_x} \sum_{x_i=1}^{N_x} [(\phi_e - \phi_t) - \text{mean}(\phi_e - \phi_t)]^2}, \quad (19)$$

where  $N_x$  is the number of measurement points,  $x_i$  are their locations and the distance  $d$  is a function of angular frequency  $d = d(\omega)$  as a result of frequency dependent properties of both the microwave antenna as well as of the spaceplate. The theoretical phase as a function of position  $x$  is given as

$$\phi_t(x) = \arg\{E(x)\} = \arg\left\{\frac{1}{r(x)} \exp(i k r(x))\right\} = kr(x) = k\sqrt{d^2 + x^2}, \quad (20)$$

where  $E(x)$  is the electric field distribution along the x-direction,  $r = |\vec{r}|$  is the distance between the phase centre and a point on the detection plane and  $k = 2\pi/\lambda$  is the free space wave number (see Fig. 12).

#### 4.4 Results of E-field spatial mapping

We present here the measured transmission phase  $\phi_e$  and normalised magnitude  $|t|/|t_{\max}|$  which are proportional to the magnitude and phase of the electric field on the measurement plane in a setup with and without the spaceplate (see Fig. 12). The phase patterns show the unwrapped phase as a function of transverse position  $x$  or  $y$  for the measurement without the spaceplate (black curves) and with the spaceplate (red/blue curves). The measurements shown in Fig. 14 correspond to two orthogonal planes where the polarisation of the wave is either TM (red) or TE (blue) with respect to the surface of the spaceplate, respectively. As a result of the apparent shift of the phase centre away from the measurement plane, we measure a shallower phase profile when the SP is introduced and a broader beam.

The plots in Fig. 13 include the information about the apparent position of the phase centre  $z_S$  calculated from the measured phase profiles using the method described in the previous section across the frequency range of 20 to 23 GHz. A more negative coordinate  $z_S$  corresponds to the source position apparently being farther away from the measurement plane.

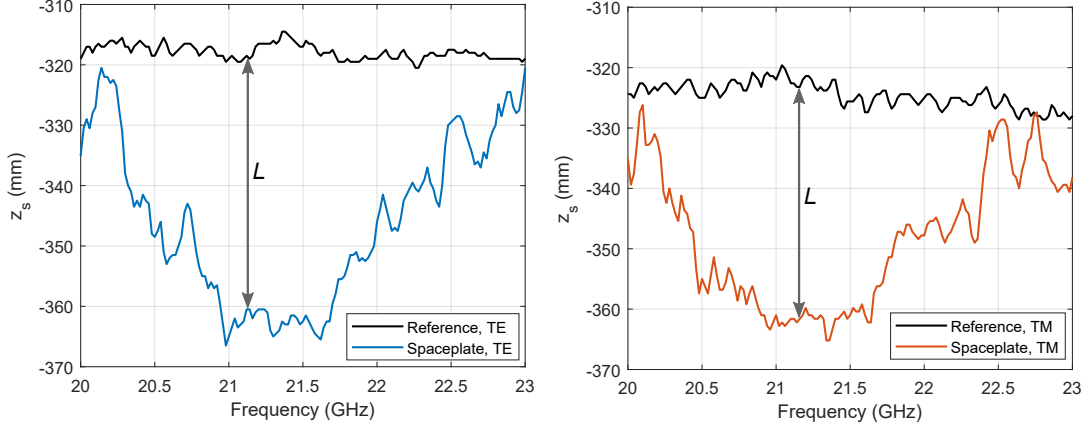


FIG. 13. Phase centre position as a function of frequency for TE (left) and TM (right) polarisation. The apparent added path length  $L$  is introduced by the spaceplate (see Fig. 1 of the main paper). The compression factor corresponding to the length  $L$  is given in Fig. 5 of the main paper.

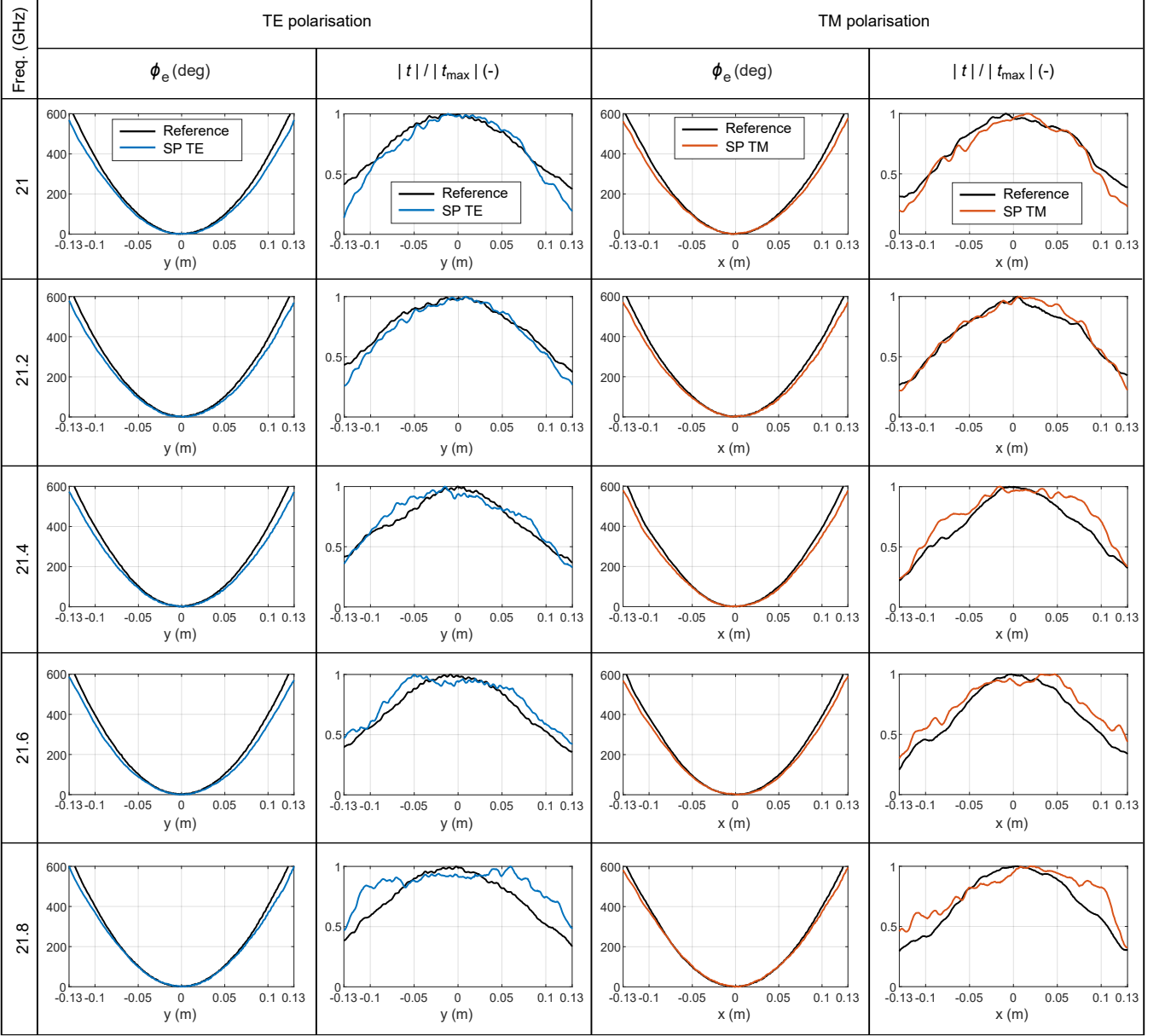


FIG. 14. Phase  $\phi_e$  and normalized magnitude  $|t|/|t_{\max}|$  of measured transmission coefficient (i.e.  $t \equiv S_{21}$ ) between an illuminating antenna and an electrically small probe on a 1D grid according to Fig. 12. The coefficient  $t$  thus corresponds to E-field on two orthogonal cuts, for TE and TM polarisation. The effect of the spaceplate on the detected phase is clear, the shallower phase profile is a direct result of spherical wavefronts with larger radius of curvature compared to the measurement without the spaceplate (black curves).

## §5 Evolutionary optimization of a stochastic spaceplate

A non-local metamaterial spaceplate can also be realised as a multilayer stack of homogeneous and isotropic layers distributed along the optical axis [9]. The parameters of individual layers – the thicknesses and refractive indices – are then optimised by a stochastic optimisation algorithm. Such a design strategy does not inherently rely on any knowledge about the behavior of the elements. Theoretically (if the search space allows it), it can take advantage of e.g. higher order modes within layers, creating multiple resonant cavities coupled by arbitrary coefficients (unlike the design in [3]) etc. However, the results of this approach presented in [9] tell us that finding a feasible solution can be quite challenging (for example in [9], with 21 layers and  $C = 4.9$ , a spaceplate with an angular range of about 12–15 deg showed transmittance below  $\sim 1.5\%$  for normal incidence). The other disadvantage is the non-scalability of the solution. Designing the spaceplate for other effective thicknesses requires, in general, starting the optimization from

a scratch. A suitable optimisation strategy could be the combination of the global search with a local gradient-based optimization method.

The problem can be formulated as either a single- or multi-objective. In our experience, the single-objective formulation with three discernable sub-objectives (amplitude, phase, compression factor  $\mathcal{C}$ ) led to a feasible solution more quickly. Generally, the objective is defined as the minimisation of the error between the desired transmission coefficient of the free space  $t_0$  and a transmission coefficient of a spaceplate  $t_{\text{SP}}$ , while the compression factor  $\mathcal{C}$  should be maximized. If we break the transmission coefficient into the amplitude and the phase derivative criterion and we sum through a finite number of incidence angles we can write for both polarisations (superscripts TE, TM)

$$\begin{aligned} OBJ = & \frac{1}{N} \sum_{\theta_i}^N c_1 \cdot (|t_{\text{SP}}^{\text{TM}}(\theta_i)| - |t_0(\theta_i)|)^2 + c_2 \left( \frac{\text{darg}(t_{\text{SP}}^{\text{TM}}(\theta_i))}{\text{d}\theta} - \frac{\text{darg}(t_0(\theta_i))}{\text{d}\theta} \right)^2 + \\ & \frac{1}{N} \sum_{\theta_i}^N c_3 \cdot (|t_{\text{SP}}^{\text{TE}}(\theta_i)| - |t_0(\theta_i)|)^2 + c_4 \left( \frac{\text{darg}(t_{\text{SP}}^{\text{TE}}(\theta_i))}{\text{d}\theta} - \frac{\text{darg}(t_0(\theta_i))}{\text{d}\theta} \right)^2 + \\ & c_5 \cdot d_{\text{SP}}/d_{\text{eff}} \end{aligned}$$

Here, the derivatives are used to remove any constraints on the global phase of the transmitted field, which is irrelevant for most of the spaceplate applications. The five weighing coefficients  $c_1 - c_5$  allow us to tune the importance of the amplitude ( $c_1, c_3$ ) and phase ( $c_2, c_4$ ) errors and the maximum achieved compression factor ( $1/c_5$ ). The inputs of the algorithm are the maximum number of the layers and the effective thickness  $d_{\text{eff}}$  which we are trying to squeeze. During the optimisation, the transmission coefficient of the free-space is pre-calculated (as it does not change during the optimisation) and the transmission coefficient of the SP is evaluated by a transfer (characteristic) matrix method [10], which gives a full-wave field solution for a multilayer stack.

In our design, we tried to reduce the search space as much as possible while still producing a solution with relatively high  $\mathcal{C}$  (in this case we set  $\mathcal{C} > 3$ ). With the experimental demonstration in mind, we opted for a two material combination with alternating high/low refractive index medium – as the low  $n$  medium, we selected air and for the high  $n$  medium a commercially available microwave substrate from Rogers ( $\epsilon_r = 10.2$ ). We fixed the thicknesses of the high  $n$  dielectric layers to 1.52 mm (thickness of the substrate). Thus, the optimization parameters are only the thicknesses of the air gaps and the total number of the layers. By allowing the thicknesses of the layers to go to zero (skipping the layer), the optimiser can effectively double the maximum thickness limitations defined during the initialisation.

In the optimisation results below, we set the frequency of operation to  $f = 15$  GHz, maximum number of layers ( $NL_{\text{max}}$ ) to 15, the effective thickness to be substituted by SP to  $d_{\text{eff}} = 250$  mm. An evolutionary optimization strategy based on a genetic algorithm in Matlab was used to search for feasible solutions. With maximum of 15 layers (8 layers of microwave substrate of fixed thickness, separated by 7 layers of air), we are optimizing only 7 parameters at most. Thus, the population does not have to be very large - we usually worked with about 100 individuals per population. On a laptop with Intel i7-7500, 2.7 GHz processor the evaluation of the forward model took on average 5 ms for both polarisations, 15 layers and a single frequency point. Evaluating the whole population thus took only about 0.5 s.

One of the optimised structures is shown in Fig. 15. We can see that the first, third and fifth gaps have lengths very close to the even FP resonances whereas the second and the fourth are relatively small. The resemblance of this stochastically optimised structure to the empirical multi-cavity design proposed in [1] is clear.

Figure 16 gives the transmittance  $|t|^2$  and the phase of the transmission coefficient for the two polarisations and compares them to the free-space fit. In Fig. 17 and 18 we can see the transmittance and the transmission phase as functions of the frequency and the incidence angle.

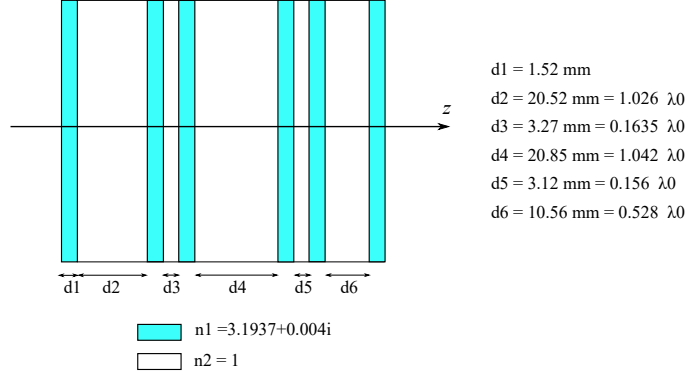


FIG. 15. Spaceplate designed by a genetic algorithm with total thickness of  $d_{SP} = 67.44$  mm substitutes a slab of air with equivalent thickness  $d_{eff} = 250$  mm corresponding to a compression factor  $\mathcal{C} \approx 3.7$ .

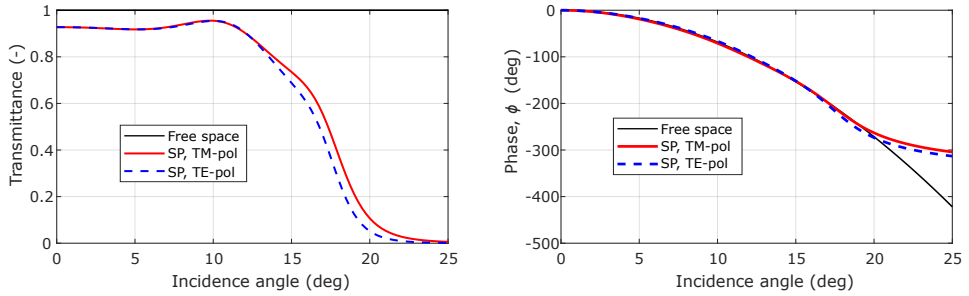


FIG. 16. Transmittance and the transmission phase of the spaceplate as a function of incidence angle at 15 GHz. The free space fit corresponds to a distance  $d_{eff} = 250$  mm.

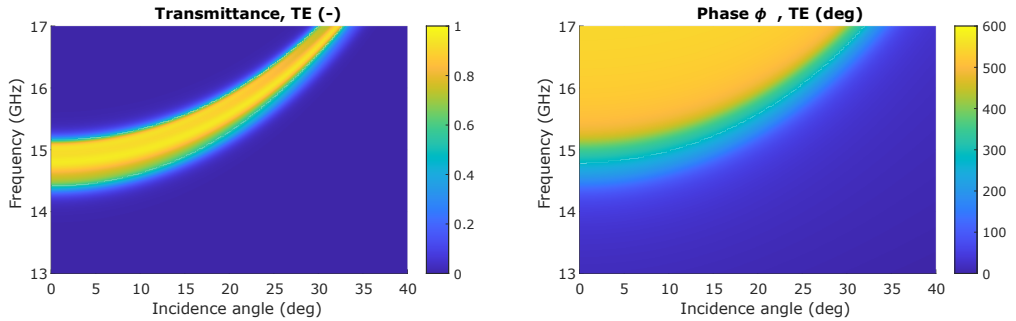


FIG. 17. Transmittance and the phase of the spaceplate as a function of incidence angle and frequency for TE polarisation.

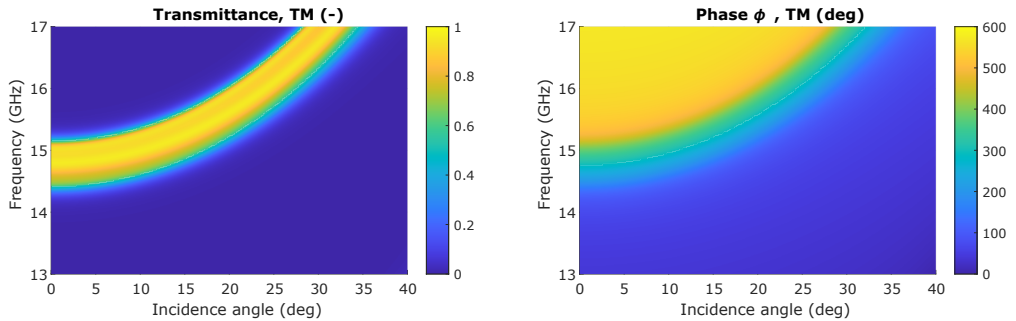


FIG. 18. Transmittance and the phase of the spaceplate as a function of incidence angle and frequency for TM polarisation.

## References

---

- [1] A. Chen and F. Monticone, “Dielectric nonlocal metasurfaces for fully solid-state ultrathin optical systems,” *ACS Photonics* **8**, 1439–1447 (2021).
- [2] K. F. Renk, *Basics of Laser Physics* (Springer Berlin Heidelberg, 2012).
- [3] J. B. Pendry, “Mimicking surface plasmons with structured surfaces,” *Science* **305**, 847–848 (2004).
- [4] F. J. Garcia-Vidal, L. Martín-Moreno, and J. B. Pendry, “Surfaces with holes in them: new plasmonic metamaterials,” *Journal of Optics A: Pure and Applied Optics* **7**, 97–101 (2005).
- [5] E. Hendry, A. P. Hibbins, and J. R. Sambles, “Importance of diffraction in determining the dispersion of designer surface plasmons,” *Physical Review B* **78** (2008).
- [6] E. K. Stone and E. Hendry, “Dispersion of spoof surface plasmons in open-ended metallic hole arrays,” *Physical Review B* **84** (2011).
- [7] C. A. M. Butler, I. R. Hooper, A. P. Hibbins, J. R. Sambles, and P. A. Hobson, “Metamaterial tunnel barrier gives broadband microwave transmission,” *Journal of Applied Physics* **109**, 013104 (2011).
- [8] G. Friedsam and E. Biebl, “A broadband free-space dielectric properties measurement system at millimeter wavelengths,” *IEEE Transactions on Instrumentation and Measurement* **46**, 515–518 (1997).
- [9] O. Reshef, M. P. Delmastro, K. K. M. Bearne, A. H. Alhulaymi, L. Giner, R. W. Boyd, and J. S. Lundeen, “An optic to replace space and its application towards ultra-thin imaging systems,” *Nature Communications* **12** (2021).
- [10] E. Hecht, *Optics* (Pearson, 2012).